SYMPOSIUM ARTICLE

Direct Numerical Simulations of a Great Horn Owl in Flapping Flight

Nikolaos Beratlis,[*,†] Francesco Capuano,[‡] Krishnamoorthy Krishnan,[§] Roi Gurka,[§] Kyle Squires[†] and Elias Balaras [iD][*,1]

[*]Department of Mechanical and Aerospace Engineering, George Washington University, Washington, DC, USA; [†]School for Engineering of Matter, Transport and Energy, Arizona State University, Tempe, AZ, USA; [‡]Department of Industrial Engineering, Universita di Napoli Federico II, Naples, Italy; [§]Department of Physics and Engineering, Coastal Carolina University, Conway, NC, USA

From the symposium "Bio-inspiration of quiet flight of owls and other flying animals: recent advances and unanswered questions" presented at the annual meeting of the Society for Integrative and Comparative Biology, January 3–7, 2020 at Austin, Texas.

[1]E-mail: balaras@gwu.edu

Synopsis The fluid dynamics of owls in flapping flight is studied by coordinated experiments and computations. The great horned owl was selected, which is nocturnal, stealthy, and relatively large sized raptor. On the experimental side, perch-to-perch flight was considered in an open wind tunnel. The owl kinematics was captured with multiple cameras from different view angles. The kinematic extraction was central in driving the computations, which were designed to resolve all significant spatio-temporal scales in the flow with an unprecedented level of resolution. The wing geometry was extracted from the planform image of the owl wing and a three-dimensional model, the reference configuration, was reconstructed. This configuration was then deformed in time to best match the kinematics recorded during flights utilizing an image-registration technique based on the large deformation diffeomorphic metric mapping framework. All simulations were conducted using an eddy-resolving, high-fidelity, solver, where the large displacements/deformations of the flapping owl model were introduced with an immersed boundary formulation. We report detailed information on the spatio-temporal flow dynamics in the near wake including variables that are challenging to measure with sufficient accuracy, such as aerodynamic forces. At the same time, our results indicate that high-fidelity computations over smooth wings may have limitations in capturing the full range of flow phenomena in owl flight. The growth and subsequent separation of the laminar boundary layers developing over the wings in this Reynolds number regime is sensitive to the surface micro-features that are unique to each species.

Introduction

Since the early days of aerodynamics, bird flight has been an inspiration to improve wing geometries, avionics, propulsion, and flow control. More recently due to the growing interest in developing unmanned air vehicles, which operate at scales closer to those occurring in avian flight, different species of birds have been studied to understand the mechanics behind their aerodynamics, flight efficiency, maneuverability, hunting strategies, and so on. A swift, for example, can stay aloft for months without landing (Hedenström et al. 2016), and Bar-tailed Godwits travel >10 km without stopping (Battley et al. 2012). One of the avian orders that has not been studied in depth from the aerodynamics perspective is predators. Some of the predators feature agile flight, high speeds, maneuverability, and stealth capabilities, given that their main food source can escape, hide, or use similar tactics to avoid becoming prey.

Owls are nocturnal predators that are using stealth capabilities to hunt their prey. Numerous studies targeting their unique silent flight capabilities have been reported. Early work done suggested that these

capabilities were attributed to their wing adaptations. The morphological features of their wings have been thoroughly characterized over the years, identifying three distinct features (Graham 1934): the leading-edge serrations, which is a comb of evenly spaced bristles along the leading edge of the wing; the trailing edge fringe of feathers; and the downy porous feathers distributed over the upper wing surface. Several studies attempted to establish a link between one or combination of these features and noise reduction (see review by Wagner et al. 2017), but as of today, the results are inconclusive. Moreover, there is no agreement if these stealth capabilities of owls are unique to this species or can be found in other avian families (Clark et al. 2020).

Some of the early work on owls' aerodynamics was done by Kroeger et al. (1972), where the aerodynamic and acoustic performances of live owls and prepared wings were tested. Anderson (1973) performed similar measurements on barn owl wing models. Both studies suggested that the wing morphological features listed above are associated with noise reduction in the expense, however, of aerodynamic performance manifested by relatively low lift-drag ratios. Later studies by Geyer et al. (2013, 2017) reached similar conclusions. Winzen et al. (2015) conducted flow measurements around prepared owl wings using Particle Image Velocimetry (PIV), and found no flow separation above the wing suggesting high lift production during flight. Direct measurements of aerodynamic forces during *in vivo* bird flight are very challenging. Lawley et al. (2019) and Nafi et al. (2020) reported near-wake flow measurements for a boobook owl freely flying in a climatic wind tunnel. The latter study verified that in comparison to other birds, the owl aerodynamic performance was low, while the former demonstrated strong turbulent suppression in the wake, which can potentially muffle its aeroacoustic (aerodynamic noise) signature.

Given the challenges and cost of conducting measurements involving live birds, it is essential to complement the current experiment-based knowledge with high-fidelity simulations. Computational fluid dynamics (CFD) is a critical component of this strategy together with methods for extracting realistic geometric representations and kinematics of birds during flight. Measuring structural properties of the wings and identifying the morphology of the surface texture and micro-features is also important. As of today, most of the modeling work on flying organisms has been focused on low Reynolds numbers, $O(10^3)$, involving insects and small birds (see Shyy et al. 2008, for a review). Song et al. (2016), for

example, conducted direct numerical simulations (DNS) of the flow induced by a hummingbird in forward flight. They used a nominal geometry representing the hummingbird and the kinematics were extracted from high-speed videos of the bird flying in the wind tunnel. The simulation revealed a highly complex wake structure and reported lift and drag forces during the flapping cycle.

For larger bird species the value of the Reynolds number increases, $O(10^4 - 10^5)$, rendering eddy-resolving, high-fidelity simulations, such as DNS is prohibitively expensive. As a result, most studies reported in the literature for larger birds adopt reduced fidelity strategies that come at a much lower cost. Ruck and Oertel (2010), for example, simulated the flow induced by a bird-inspired model at realistic Reynolds numbers. The wings were elastic membranes and their kinematics simplified to a sinusoidal rotation about two axes. To reduce the computational cost the Reynolds Averaged Navier Stokes (RANS) formulation was adopted coupled to the widely used $\kappa - \omega$ turbulence model. The commercial solver, Fluent, was utilized and the results were in broad qualitative agreement with experimental observations. Lower fidelity tools have also been used to further reduce the cost in high Reynolds numbers. An example can be found in the study by Gardiner et al. (2013), where barnacle geese at high-speed migrating flight were considered. The wing geometry and camber were obtained from three-dimensional scans of a dried wing, while video footage from wind tunnel experiments was utilized to extract the wing kinematics. The airflow was then modeled using an unsteady vortex lattice (UVL) method. The wake structure was in broad agreement with the experimental observations, but the predicted lift force was excessive as UVL methods cannot account for separation.

The fidelity of the fluid flow solver, however, only partially determines the overall accuracy of the simulation. The accuracy in extracting the unique wing kinematics resulting from the mechanical motion of the wing, as well as their flexibility are important as these have a great impact on the aerodynamic forces that assist the avian flight performance (Tobalske et al. 1999; Hedrick et al. 2004; Liu et al. 2006; Rosén et al. 2007; Henningsson et al. 2008). To the best of our knowledge, flow simulations around owls during flight have not been reported yet. Most of the related computational work has focused on wing morphological features specific to owls that have been incorporated into idealized wing models. Agrawal and Sharma (2016) investigated the noise emission from an airfoil, typically used in wind

turbines, modified by various leading edge serrations using the open source finite volume solver OpenFoam (2007). They show a distinct noise reduction using these modifications. Kondo et al. (2014) analyzed the aerodynamic loads exerted by an owl-like airfoil in idealized flow conditions (two-dimensional laminar flow). Other works were based on potential flow assumptions (Ford and Babinsky 2013; Ben-Gida et al. 2020) where the flow field is assumed to be irrotational, steady, and viscous forces are negligible.

In this work, we report DNS of the flow induced by the flapping flight of a great horned owl (GHO). We present a novel approach to extract the kinematics from experiments with live owls as well as a highly efficient Navier–Stokes (NS) solver that enables such computations at realistic Reynolds numbers. The model of the flapping owl is assumed to have a smooth surface, where the no-slip and impermeability boundary conditions are directly enforced with an immersed-boundary method. The surface micro-features that are specific to owls are not considered. Introducing the latter requires sophisticated multi-scale modeling strategies guided by coordinated experiments, which is beyond the scope of this work. Our objective is to establish the baseline flow field induced by the smooth surface approximation at realistic Reynolds numbers and kinematics that can, indirectly by comparisons to experimental studies, point to their importance in the overall wake structure. In the next section, we will outline the methods, followed by the results and discussion.

Methods

Flight tests

GHOs (*Bubo virginianus*) are one of the most common owls of the Americas and are generally large, thick-bodied with broad and rounded wings (König and Weick 2008). They are nocturnal and known to be aggressive and powerful during hunting. The owl tested was brought from the African Lion Safari in Cambridge, ON, Canada to the Advanced Facility for Avian Research (AFAR) at the University of Western Ontario, London, ON, Canada under animal protocols from the University of Western Ontario Animal Care Committee (UWO #2010-216) and the African Lion Safari (BOP-15-CS). It was sheltered at AFAR for 2 weeks before the experiments, weighed every day, and trained to fly at the wind tunnel on daily basis.

Given the size of the bird, we have flown the owl in a large open wind tunnel in a perch-to-perch flight mode. In particular, the Boundary Layer Wind Tunnel I (BLWT-I) was utilized, which is an open circuit tunnel with dimensions of 33 m length, 2.4 m width and varying height of 1.5–2.15 m (from the entrance to the test area). The turbulence intensity in the tunnel was measured to be ~5.8%. The pressure, temperature, and the humidity conditions during the experiments were at standard atmospheric level. The bird was initially perching on the trainer's hand who was located downstream far away from the measurement location (see Fig. 1) and was gently tossed into the oncoming flow (head wind) flying toward the perch for food which was placed upstream. The wind tunnel speed of the oncoming flow was to ~3 m/s.

The flights were performed during dark conditions since part of the experiments included PIV measurements. Therefore, only the light directly above on the landing perch was left in use for the bird to locate and land on the perch. In order to ensure the bird safety during flight, a set of opto-isolators comprised of six IR transceivers were integrated with the PIV system (located upstream away from the laser sheet location), which prevented the direct contact between the bird and the laser sheet (Kirchhefer et al. 2013). The laser light sheet was shot only when the bird flew through the IR transceivers system. During the flights that were conducted over the course of 2 days, the bird was consistently released from ~1.7 m from the floor (the shoulder level of the trainer). The typical flight path employed by the bird during the experiments is shown in Fig. 1. It was observed that the bird adapted the same flight path and behaved almost in the same fashion during each flight. Table 1 provides the details of the weight, geometrical measurements, average bird speed, and the Reynolds number during the experiments.

In addition to the time-resolved PIV system which was utilized for flow measurements (Taylor et al. 2010), four GoPros and three mobile phone cameras were used to capture the bird kinematics from multiple views. A detailed schematic of the overall setup is shown in Fig. 1. The shaded represents the area where we performed the flow measurements. The wind was blowing from right to left while the birds were flying upstream against the wind from left to right. One of the PIV high-speed cameras was used for the wake flow field measurements and the other camera was used for capturing the wingbeat kinematics of the bird, simultaneously. All other cameras (GoPros and mobile phone) recorded videos of the bird flight from both sides, top and bottom of the wind tunnel around the infra-red sensor location. In the manuscript, we will primarily report the kinematics extracted from these experiments, which are
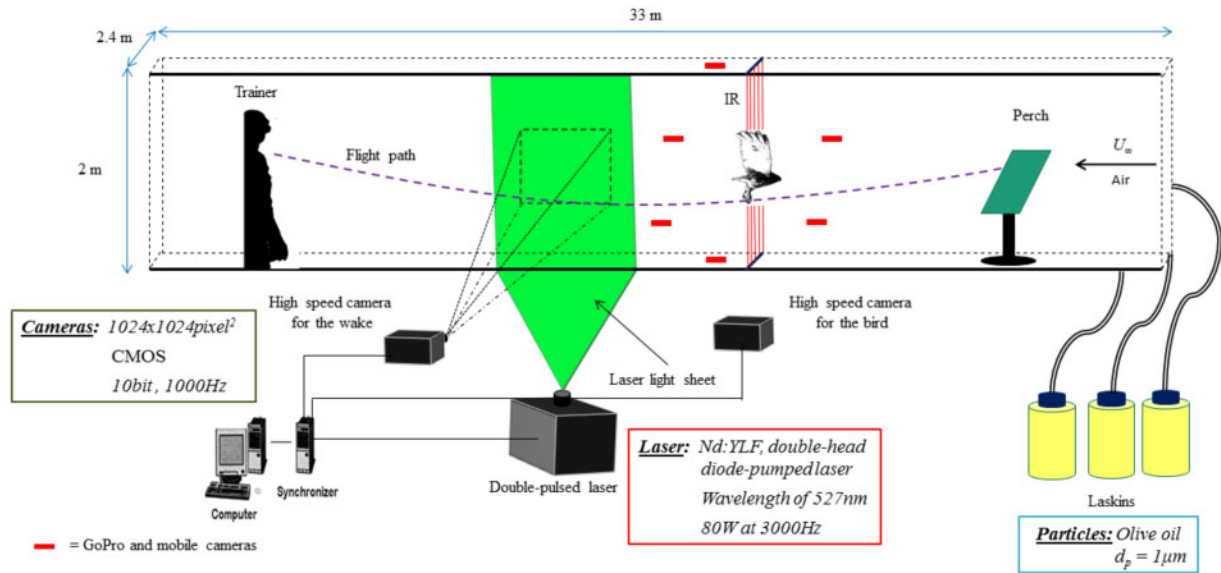
Fig. 1 Schematic of the experimental setup at BLWT-I.

Table 1 Specifications of the bird, average speed, and Reynolds number

Mass (g)	Body length (cm)	Half wingspan (cm)	Mid chord (cm)	Bird speed (m/s)	Reynolds number
1199	45	57	19	5.2	67,700

central to the development of the high-fidelity flow simulation tool that is the focus of the study.

Computational approach

To capture the highly complex three-dimensional separated flow generated by an owl in flapping flight we adopt a DNS approach. In such case, the NS equations for incompressible flow are solved on a computational grid that is sufficiently fine to resolve all scales down to the Kolmogorov scale (see e.g., Moin and Mahesh 1998). However, directly resolving the detailed texture and/or micro-features (order of mm), on the wing's surface (order of m) is prohibitively expensive and can only be possible through multiscale modeling strategies. The downy coating for example, which is practically a filamentous layer with ∼70% open area can be modeled as poroelastic material with microscopic physical properties such as permeability, effective elasticity, and bulk compliance of the solid skeleton, which are then introduced in a macroscopic model (see Skotheim and Mahadevan 2004). The present work considers smooth impermeable wing surfaces and does not attempt to account for any of the micro-features. Our plan is to establish the baseline structure of the wake and resulting aerodynamic forces produced by a smooth wing platform, which will serve as a reference for future

multiscale simulations and experiments that may include one or more of the owl specific micro-features.

The computation of the flow in the presence of solid boundaries undergoing large displacements is very challenging, even for smooth surfaces (i.e., herein wings). In our approach, the geometry of the owl is represented by a Lagrangian grid consisting of triangular elements (see Fig. 3d), which is immersed in a fixed Cartesian grid, where the equations governing the flow dynamics are solved. The requirement for the Eulerian grid to conform to the body is relaxed, and the nonslip boundary conditions are imposed using the immersed-boundary formulation proposed by Balaras (2004) and Yang and Balaras (2006). The overall method can be summarized in the following steps: (1) All computational points on the fixed Eulerian grid are classified according to their relation with the solid body using a ray-tracing technique. For example, a ray is shot in the vertical direction and all the intersections with the triangles are found as shown in Fig. 2a. Any Eulerian point along a gridline that lies between an odd and even intersection is part of the solid, while all the ones outside the solid are part of the fluid; (2) The velocity field at the forcing nodes (all fluid points that have at least one neighbor in the solid) is reconstructed using linear interpolation in order to satisfy the boundary conditions on the solid body.
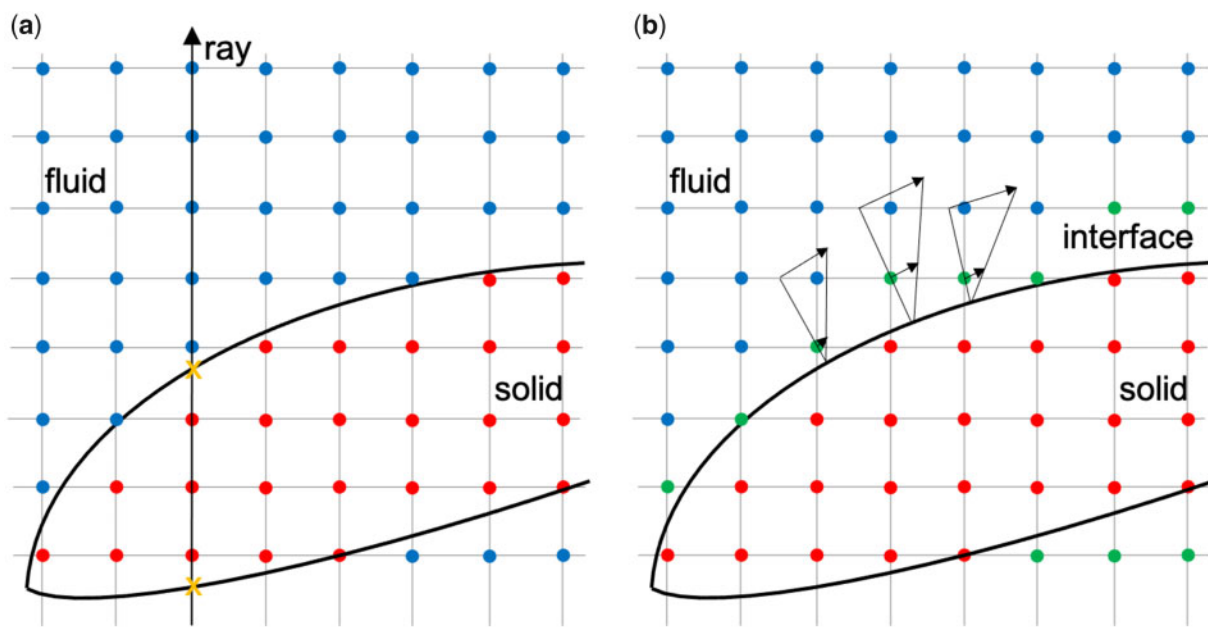
Fig. 2 Immersed boundary method overview (**a**) ray tracing to classify fluid and solid points (**b**) interpolation stencil on forcing points.
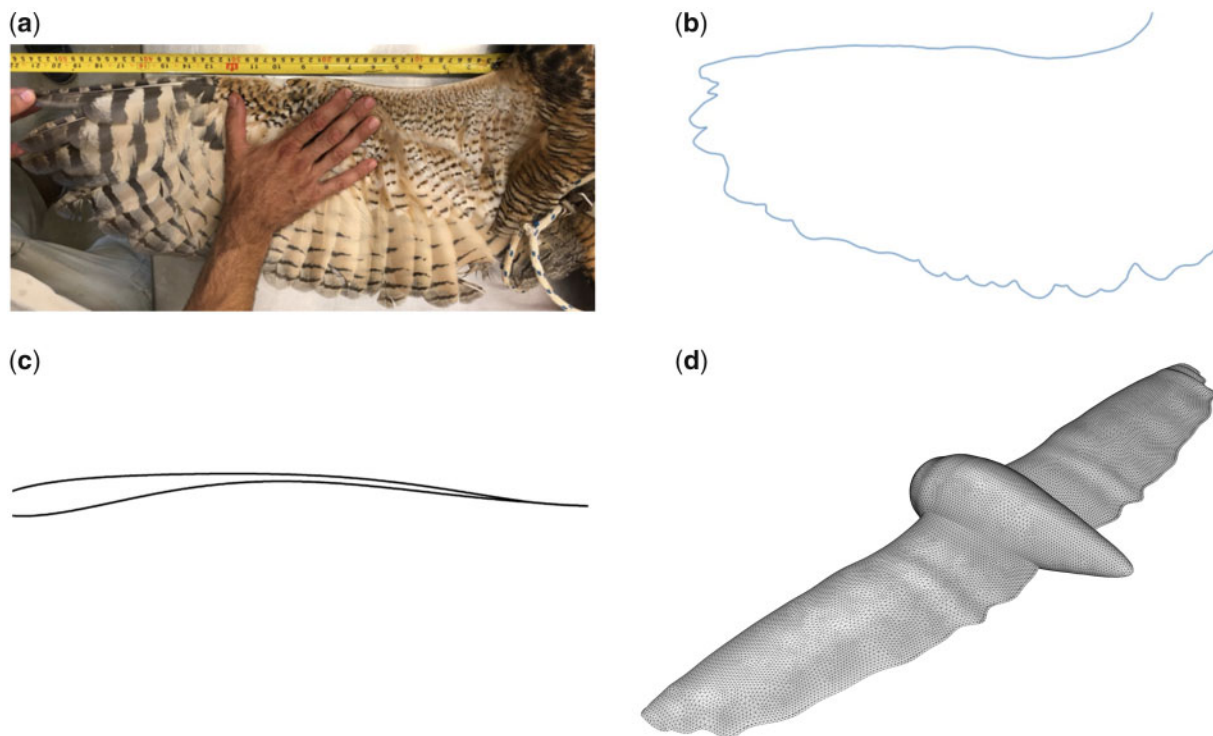

Fig. 3 (**a**) Photograph of the owl wing planform; (**b**) Extracted profile of the wing planform from the photograph; (**c**) Profile of the owl airfoil extracted from Liu et al. (2006); (**d**) Reconstructed three-dimensional model.

The equations governing the fluid flow are advanced in time using a semi-implicit projection method, where all terms treated explicitly are advanced using a third-order Runge–Kutta scheme, and all terms treated implicitly are advanced using a second-order Crank–Nicholson scheme. All spatial derivatives are discretized using second-order central-differences on a staggered grid. The code is parallelized using a domain decomposition approach with excellent parallel performance on leadership high-performance computing resources. Details on the overall method together with a demonstration
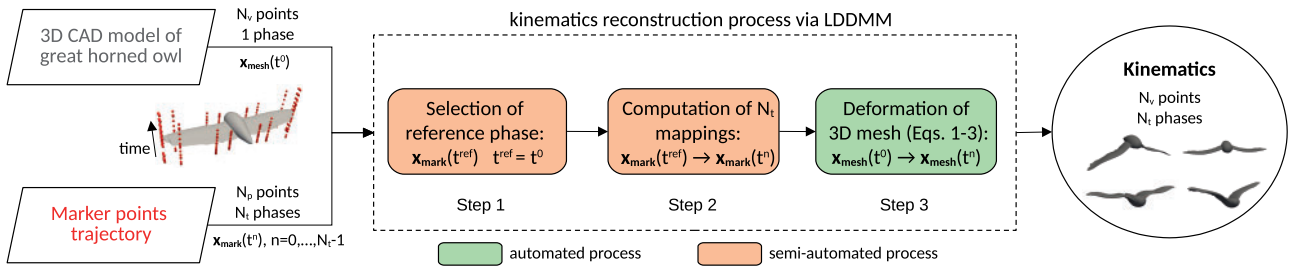
Fig. 4 Flowchart describing the kinematics reconstruction process.

of the formal accuracy of the solver in space and time can be found in Balaras (2004) and Yang and Balaras (2006). The solver has been extensively validated for external flow problems covering the Reynolds number range considered in the present work. Examples include flapping foils (Rahromostaqim et al. 2016), rotating foils (Posa et al. 2016; Posa and Balaras 2018), and bluff bodies (Posa and Balaras 2016; Pal et al. 2017).

Model geometry and kinematics

In the DNS reported below, central in reproducing the flow features induced by the owl in perch-to-perch flight considered in the experiments, is the fidelity of the geometrical model and kinematics during the flapping cycle. In this section, we will discuss a novel approach to achieve this task, where the kinematics of a limited set of points on the wing's surface extracted from images captured by a set of cameras during the experiments are used to animate a detailed CAD model of the owl using an atlas-driven, image-registration technique.

CAD model of the great horn owl

Following the experiments, the GHO returned to the African Lion Safari, where we were able to perform a full-scale measurement of the GHO while the wings were fully opened. We measured the spanwise length of the wing planform, wing root, wing tip, body sizes, and photographed the wing planform of the bird. Based on these measurements, we reconstructed a three-dimensional model of the GHO using Solidworks (Dassault-Systemes). It should be noted that we replicated the geometry and dimensions of the wing planform, but we did not include the wing and body feathers. We manually traced the wing planform of the owl with numerous closely placed points and rescaled it with its actual physical scale. Pictures of the actual wing and the extracted profile are shown in Fig. 3a and b, respectively. A generic owl airfoil based on the one reported by Liu et al. (2006) was utilized. We then traced and extracted the airfoil section manually and used XFLR5 (X-

Foil) to smooth the model using a fit spline curve. The extracted airfoil section is shown in Fig. 3c. We measured the varying chord length along the wing planform at multiple locations and scaled the airfoil with the relevant chord distributions. This information was used to build the wing with chord length and thickness distribution by stacking the airfoils sections in the spanwise direction. A replica of the left wing is reconstructed from the right wing and the complete bird model was assembled as shown in Fig. 3d.

CFD-ready kinematics of the CAD model

The GHO model discussed above is stored in standard stereolithography (STL) format, and it consists of a number of nodes and triangles defining its surface. The evolution in time during the flapping cycle of the coordinates, velocities, and accelerations of all triangles in this data-structure is the input to the immersed-boundary CFD solver. Given that the experiments only provide the kinematics of a few strategically placed markers on the wings, we developed a novel approach to define the kinematics of the full STL file based on this information. The overall process is succinctly depicted in the flowchart reported in Fig. 4, and described in detail in the following.

Let us assume we have a discrete set of N_p markers with spatial coordinates $\mathbf{x}_{mark}$, placed along the wingspan (i.e., Fig. 7). A finite number of time instances N_t of the markers motion in the form of point clouds is available, indicated as $\mathbf{x}_{mark}(t^n)$, with $n = 0, \ldots, N_t - 1$; note that t^0 corresponds to the physical time $t/T = 0$. Given the spatial and temporal coarseness of the markers, standard multi-dimensional interpolation techniques may suffer from strong under-determination, and thus fail to provide a high-fidelity description of the kinematics. Furthermore, the triangulated surface mesh required by the CFD solver should have a consistent topology and preserve its connectivity properties during the flapping cycle, so to ensure compatibility with the immersed-boundary algorithm; these properties are

in general not satisfied by standard interpolation procedures. Therefore, the idea followed in this work is to use the markers motion to drive the deformation of a spatially finer representation of the wing, by means of an image-registration technique.

In particular, we utilize an atlas-driven, image-registration technique based on the large deformation diffeomorphic metric mapping (LDDMM) framework (Beg et al. 2005; Durrleman et al. 2014). This approach has been used primarily in the context of biomedical applications to analyze shape variations of living organs in response to pathologies (i.e., Mansi et al. 2011). The main advantage of using the LDDMM approach is that it provides a smooth global mapping, and is constructed in such a way to inherently preserve the topology of surfaces, thus avoiding singularities or self-intersections of the surface mesh even for large deformations. In this framework, the time evolution of a generic set of points, $\mathbf{x}$, is parametrized by a sparse combination of a discrete set of, N_c, control points, $\mathbf{c}_p$, and corresponding momenta, $\boldsymbol{\alpha}_p$, as follows:

$$\mathbf{x}.(t) = \sum_{p=1}^{N_c} K\left(\mathbf{x}, \mathbf{c}_p(t)\right) \boldsymbol{\alpha}_p(t), \qquad (1)$$

where K is a Gaussian kernel $K(x, y) = \exp\left(-||x - y||^2/\sigma_\nu^2\right)$, and σ_ν is a parameter controlling the width of the kernel. Use of Equation (1) allows to compute a transformation (registration) between an initial reference state $\mathbf{x}^{\mathrm{ref}}$ and a target state $\mathbf{x}^{\mathrm{targ}}$, through specification of $\mathbf{c}_p(t)$ and $\boldsymbol{\alpha}_p(t)$. In turn, the control points and momenta evolve according to:

$$\mathbf{c}._q(t) = \sum_{p=1}^{N_c} K\left(\mathbf{c}_q, \mathbf{c}_p(t)\right) \boldsymbol{\alpha}_p(t), \qquad (2)$$

$$\boldsymbol{\alpha}._q(t) = -\sum_{p=1}^{N_c} \boldsymbol{\alpha}_q^T \boldsymbol{\alpha}_p \nabla_{\mathbf{c}_q} K\left(\mathbf{c}_q(t), \mathbf{c}_p(t)\right). \qquad (3)$$

It is easy to check that the dynamics of the entire system Equations (1)–(3) is completely determined by the initial state $\mathbf{S}(0) = \{\mathbf{c}(0), \boldsymbol{\alpha}(0)\}$. Indeed, given the initial conditions $\mathbf{S}(0)$, Equations (2) and (3) can be integrated to yield the complete evolution of $\mathbf{c}(t)$ and $\boldsymbol{\alpha}(t)$, which in turn allows integration of Equation (1). Computing the transformation is an optimization process that consists in finding the state $\mathbf{S}(0)$ that minimizes the Euclidean distance between the target and the integrated reference states.

As stated above, the idea is to deform a fine representation of the wing according to the motion of the markers. This is achieved using a three-step procedure:

Step 1: A reference (or atlas, i.e., mean) configuration of the markers $\mathbf{x}_{\mathrm{mark}}(t^{\mathrm{ref}})$ is selected. Given the relatively symmetric motion, the configuration $\mathbf{x}_{\mathrm{mark}}(t^0)$, corresponding to $t/T = 0$, is considered as the reference one. Alternatively, the procedure proposed in Gori et al. (2017) can be used to compute an atlas in a meaningful statistical sense.

Step 2: A total of N_t transformations are computed, from the reference configuration $\mathbf{x}_{\mathrm{mark}}(t^0)$ to each of the instances, $\mathbf{x}_{\mathrm{mark}}(t^n)$. This amounts to computing N_t states $\mathbf{S}^n(0)$, with $n = 1, \ldots, N_t$. Upon integration of the system Equations (1)–(3) with initial conditions $\mathbf{S}^n(0)$, the point cloud of markers $\mathbf{x}_{\mathrm{mark}}(t^0)$ is transformed into (an approximation of) $\mathbf{x}_{\mathrm{mark}}(t^n)$. The LDDMM implementation available in the open-source software deformetrica (Deformetrica) is used to derive the transformations. As a pre-processing step, each of the point cloud $\mathbf{x}_{\mathrm{mark}}(t^n)$ is spatially refined from $N_p = 7$ to $N_p \approx 100$ using standard interpolation tools available in MATLAB to increase the accuracy of this process. The kernel width, that controls the length scale of the deformation, is selected based on the owl wingspan and qualitative observation of the experimental wing motion. After several preliminary tests, we set the kernel width to $\approx 1/6$ of the owl wingspan, which turned out to provide a good compromise between accuracy (i.e., difference between the deformed surface mesh and the marker points) and smoothness of the resulting wing motion. Smaller kernel widths tended to yield an unrealistic wavy wing shape, while a larger kernel width resulted in a stiff deformation that could not match the markers accurately.

Step 3: The computed transformations are used to deform a fine spatial model of the owl in the reference configuration, which consists of a standard surface mesh with N_ν nodes. In the results reported in this article, the model shown in Fig. 7 has approximately $N_\nu \approx 50000$ nodes. The set of nodes $\mathbf{x}_{\mathrm{mesh}}$ is integrated through Equation (1) using the parameters computed in Step 2. As a result, N_t instances of this mesh sharing the same topology (number of nodes and connectivity) are generated. The outcome of the process for four time instances in the flapping cycle is shown in Fig. 5.

Finally, a time-continuous representation is obtained via linear interpolation of the points $\mathbf{x}_{\mathrm{mesh}}(t^n)$.

Results

Kinematics of the owl wing

As we discussed in the experimental setup above, imaging was obtained in a fixed window, with the owl flying away from it, toward the upstream perch. During this time, a high-speed camera, GoPro and mobile phone cameras recorded continuously ∼20–30 min during the experiments each day. Measurements were conducted over several flights. The time evolution of spatially averaged u and v flow velocities in the wake of the owl are shown for four of the flights in Fig. 6 obtained from PIV measurements. Each flight is named as scene with a number. The evolution of the velocities is consistent with the experimental conditions: the owl is flying away from the fixed window and the earlier times correspond to the flow induced by the bird close to
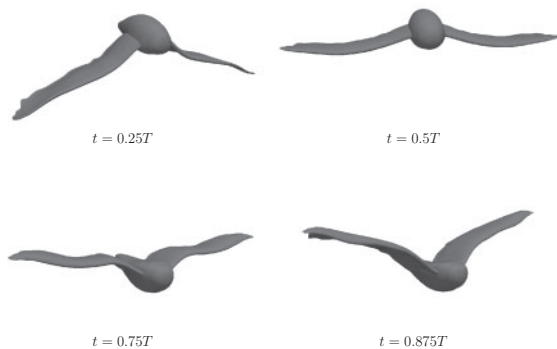
the measurement field of view. It can be seen that the owl completes at least one flapping cycle close to the field of view and then soars/glides farther upstream to the perch. Focusing at the clear cycles (i.e., $t/T < 2$), it can be observed that the flow decelerates at one half of the cycle and accelerates at the latter half. The v velocity evolution indicates that the bird typically sinks close to the measurement location and soars upstream.

The above behavior was taken into consideration when manually processing the footage from the GoPro and mobile phone cameras to identify the birds' motion for each individual flight. Then, images were extracted from these flight videos to obtain the kinematics. Birds in general exhibit complex three-dimensional wing movements during flapping flight. Here, we extract a set of simplified wing kinematics which replicates the flapping movement during flight. We used images of the spanwise plane captured from the sides of the wind tunnel, to extract the vertical translations of the wingbeat movement. We assumed that for the prescribed wingbeat cycle, the bird was flying at constant speed and maintained altitude. We selected seven locations (see, Fig. 7a) along the wing to extract their vertical displacement over single wingbeat cycle: three locations at the leading-edge (at 10% of span (P1), 30% span (P2), and 80% span (P3) measured from the root); three locations at the trailing edge (at 10% of span (P7), 30% span (P6), and 80% span (P5) measured from the root); and one at the wingtip (P5). These points were not marked using dye before the experiments, but rather identified and tracked manually over the consecutive kinematics images for the wingbeat cycle. A motion analysis software Kinovea (https://www.kinovea.org/) was used to extract the

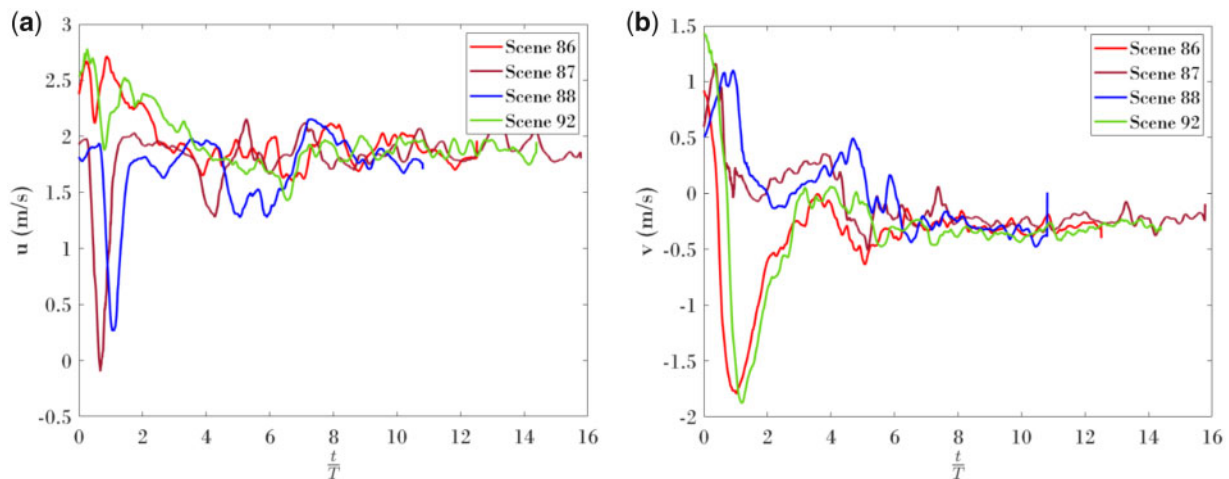**Fig. 5** Results of the kinematics extraction at four points of the oscillation period.

Fig. 6 (a) Spatially averaged *u*-velocity time series; (b) Spatially averaged *v*-velocity time series. The *y*-axis represents the respective quantity and the *x*-axis represents time normalized by the wingbeat period, *T*.
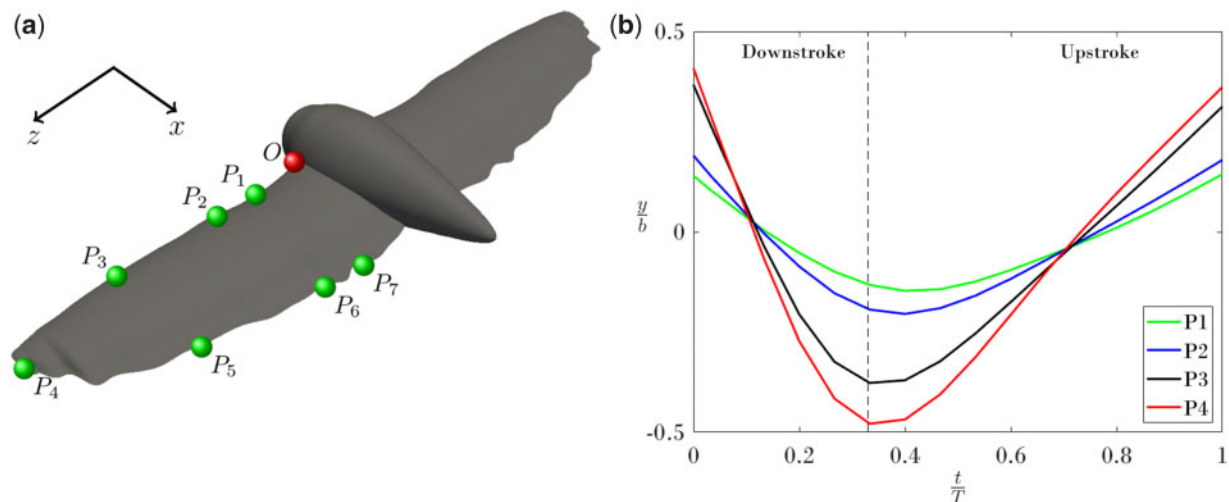
Fig. 7 (a) A model of the GHO with marker points. Points marked to represent the locations where wing kinematics were traced. P1, P2, and P3 are on the leading edge at 10%, 30%, and 80% of span from the root (origin), respectively. P4 is at the center of the wingtip. P5, P6, and P7 are on the trailing edge at 80, 30, and 10% of the span from the root, respectively; (b) Extracted wingbeat kinematics at marker points P1, P2, P3, and P4 (T is the wingbeat period, and b the half-wingspan).

coordinates (x and y) of these marker points for each consecutive image. The extracted y-coordinates helped us to reconstruct the flapping wing movement along the vertical direction. The kinematics traced at the marker points P1, P2, P3, and P4 are shown in Fig. 7b (the kinematics for markers P7, P6, and P5 are similar to the ones of P1, P2, and P3, respectively, and are omitted for clarity). The translational amplitudes of the vertical displacement, y, are nondimensionalized with the half-wingspan length, b, of the owl. The x-axis in Fig. 7b corresponds to the wing translational timestep, t, nondimensionalized with the wingbeat period, $T = 0.25$ s. The trend of the wingbeat cycle appears to be similar between the marker points. The peak-amplitude registered by the wingtip (P4) is ∼0.4 times half-span length. In addition, the wingbeat phases are identified: the downstroke and the upstroke. The owl exhibits steep downstroke and relatively longer upstroke.

Numerical simulations

Setup and parametric space

The computational domain is shown in Fig. 8a. The streamwise, vertical, and spanwise directions are denoted by x, y, and z, respectively. The domain measures $12L_c \times 11L_c \times 11L_c$ in the x, y, and z directions, respectively, where L_c is the average wing cordlength. The inflow is located $1.5L_c$ from the front of the wings. The sensitivity of the flow to grid resolution was assessed by performing simulations on three computational grid with increasing resolution

hereinafter referred to as: (1) coarse with $1000 \times 623 \times 2000$ points (1.25 billion); (2) medium with $1502 \times 887 \times 3000$ points (4.0 billion); (3) fine with $2002 \times 1246 \times 3000$ points (7.5 billion) in the x, y, and z directions, respectively. Note that the fine grid has the same resolution in the spanwise direction as the medium one, while is 50% finer in the cross-stream plane. For all cases, the grid around the owl is approximately uniform with an aspect ratio close to 1 as is shown in Fig. 8b, and was designed to properly capture the thin boundary layers and detached shear layers near the surface of the wing. For the medium grid for example, there are ∼270 points along the average chord length of the wing, 50 points across the maximum wing thickness, and 400 points along the wing span. Between 8 and 10 points are placed at the attached boundary near the leading edge of the wing.

The Reynolds number was set to Re $= U_\infty L_c/\nu = 50{,}000$ (U_∞ is the freestream velocity, and ν the kinematic viscosity). The corresponding Strouhal number was St $= fA/U_\infty = 0.25$, where f is the flapping frequency and A is the peak-to-peak cross stream amplitude of the wing motion. The reduced frequency was $f_r = \pi f L_c/U_\infty = 0.4$. At the inlet a uniform velocity profile is specified and at the outflow the convective boundary condition proposed by Orlanski (1976) is used. The latter utilizes the one-dimensional wave equation at the outflow boundary to convect all the turbulent eddies out of the computational box. In the spanwise direction, periodic boundary conditions are used, while at the freestream boundary a free-slip condition is enforced.
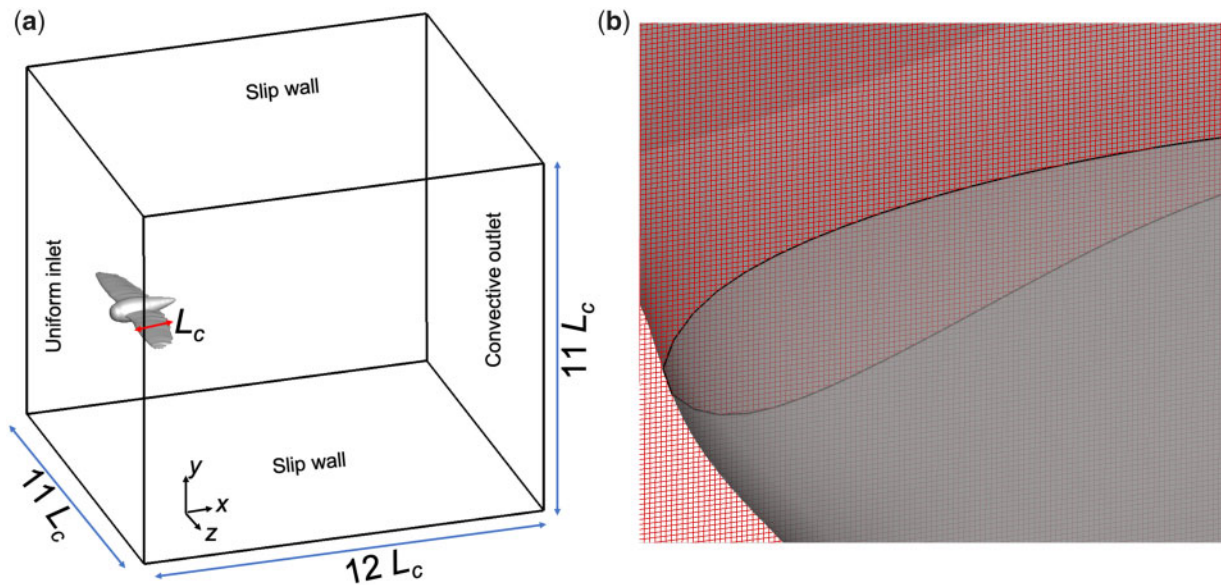
Fig. 8 (a) Outline of the computational domain. (b) Grid around the wing of the owl.

The computations on the coarse grid were initialized with a uniform flow field. After three wingbeats, equivalent to one and half flow-through times, the aerodynamic forces reached a quasi-periodic state. To reduce the transient time required to reach the latter, the computations on the medium and fine grids were initialized with an instantaneous realization from a coarser grid interpolated on the current one. The computational cost for each case is a function of the grid resolution. A typical simulation on the medium grid, for example, takes a total of 500,000 CPU hours. All our computations were run in parallel on the Pegasus High Performance Computing Cluster at the George Washington University: using 1000 Intel Xeon E5-2670 2.6 GHz cores, it takes approximately 2 days for one flapping cycle to be completed, which corresponds to 10,000 time steps.

Wake structure and aerodynamic forces

Before discussing in detail the aerodynamic forces and wake structure we will examine the effects of the grid resolution on the results. Figure 9a shows the history of the force coefficients,

$$C_D = \frac{F_{\text{drag}}}{0.5 \rho U_\infty^2 A_p}, \quad C_L = \frac{F_{\text{lift}}}{0.5 \rho U_\infty^2 A_p} \quad (4)$$

where $A_p = L_c \times L_z$, is the average planform area of the wing (L_c and L_y are the maximum chord length and wing span, respectively) and ρ is the density of the air. The drag, F_{drag}, and the lift, F_{lift}, forces are computed by direct integration of the

hydrodynamics stresses on the surface of the whole owl. We should note that the computation of the hydrodynamic forces for the case of immersed boundary methods is not trivial, as the body surface and grid lines are not aligned. Details on the different strategies that can be used for computation of these forces in immersed boundary formulations, including the one utilized in the present work, together with a detailed validation for benchmark problems can be found in Wang et al. (2019). Validation for the case of thin airfoils for the same Reynolds number range considered in this work has been reported by Rahromostaqim et al. (2016) and Posa et al. (2017). In particular, the flow over an Eppler 387 airfoil was considered at Reynolds number, $\text{Re}_c = 3 \times 10^4$ (based on the freestream velocity and the airfoil chord length), for various angles of attack, as well as pitching modes. The computed aerodynamic forces were within 2% of the experimental results reported by Yang and Spedding (2013) for the same problem.

Figure 9a clearly indicates that the forces are not dramatically affected by the grid resolution. In particular, the difference in the pick lift coefficient at the beginning of the downstroke between the medium and fine grids is <3%, while the coarse grid predicts a 7% lower pick. The average lift coefficient during one flapping cycle for the medium and fine grids is also within 3.5%, while the difference of between the coarse and fine grids is 12.5%. The drag coefficient on the other hand is less sensitive to numerical resolution and the cycle average for all grids is within 2%. To get a better understanding of
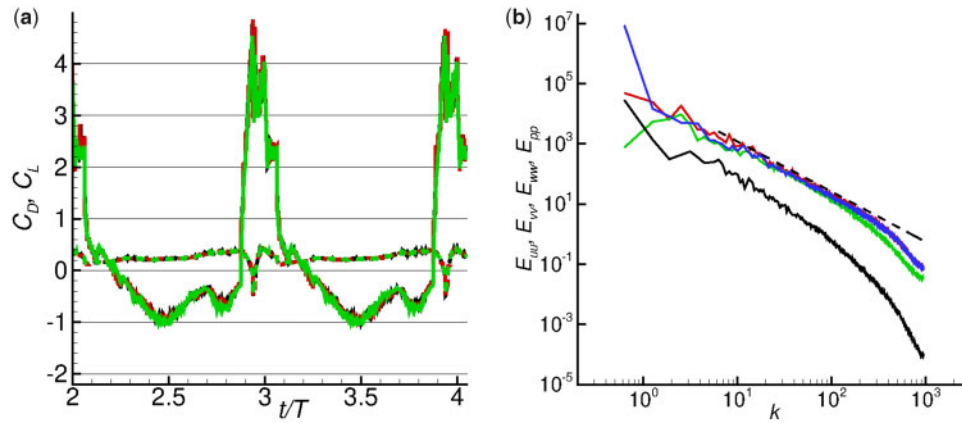
Fig. 9 (a) Effect of grid refinement on the time history of drag, C_D, and lift, C_L, coefficients. $-$ — C_D coarse grid; — $-$ C_D medium grid; $- - - C_D$ fine grid; ——— C_L coarse grid;—·— C_L medium grid;—·— C_L fine grid. (b) One-dimensional energy spectra were taken along the span at the one chord length behind the owl for the medium grid: ——— E_{uu}; ——— E_{vv};——— E_{ww};——— E_{pp}; $-- - - -5/3$ slope.

the range of scales captured by the computational grid one-dimensional energy spectra of the velocity and pressure fluctuations taken along the spanwise direction at one chord length behind the owl were also computed (see Pope 2011). An example is shown in Fig. 9b for the medium grid, where the dashed line represents the $-5/3$ slope which is typical of the inertial subrange in turbulent flows. It is clear that an extensive inertial subrange is captured with an acceptable drop-off at high frequencies, confirming that the small scales are adequately represented. We also estimated the Kolmogorov length scale, $\eta = (\nu^3/\epsilon)^{1/4}$ (where ϵ is the rate of energy dissipation) at the same location, which was found to be approximately, $\eta \sim 2 \times \Delta x_i$ (Δx_i is the local grid size). This ratio of $\eta/\Delta x_i$ is on par or better than the majority of DNS reported in the literature for wake flows. We can therefore consider the results on the medium grid to be minimally effected by further grid refinement, and we will discuss them in more detail below.

Figure 10 shows the evolution of the drag and lift coefficients over one wingbeat cycle for the medium grid. The y-coordinate of the wing tip is also shown (black dashed-line) for phase reference. In all our computations, the aerodynamic forces always attain a quasi-periodic state after approximately two wingbeat cycles. The drag force remains almost constant throughout the entire wingbeat except during the transition phase from upstroke to downstroke, where a sharp drop is observed. This observation is in qualitative agreement with the experimental observations by Nafi et al. (2020), where the variation of the drag force extracted from PIV measurements in the wake of a boobook owl flying freely and steadily in a wind tunnel was reported. The mean value of the drag coefficient is $C_D^{mean} = 0.12$.

The lift coefficient, which is also shown in Fig. 10, hits a maximum, $C_L^{max} \sim 5.0$, also during the transition phase from upstroke to downstroke and remains positive during the entire downstroke portion of the flapping cycle. A second peak is also observed early in the downstroke phase. During this part of the cycle the produced lift force is comparable to the weight of the owl. Using Equation (4) and Table 1, for example one can compute the peak lift force to be $\sim 12.2 \text{Kg} \, m \, s^{-2}$ As the wing kinematics transition to the upstoke part of the cycle, the lift coefficient drops drastically and remains negative, $C_L^{min} \sim -0.05$ for most of this phase. As a result, the average lift coefficient for the full flapping cycle drops to, $C_L^{ave} \sim 0.11$. The latter appears to be low if one compares it to weight of the owl, but we also need to consider the following: (1) the kinematics driving these computations have been extracted from perch-to-perch flight in the wind tunnel, and the owl after taking off from the handler's hand, completed two flapping cycles before gliding toward the second perch (see Fig. 1). Contrary to steady flapping flight, where one can assume that the average lift force produced during a flapping cycle is comparable to the weight of the bird, in this case, part of the energy required to maintain the particular flight path is generated during the release and the owl may adapt its wings' kinematics to generate less lift; (2) the wings and body are approximated by smooth surfaces, where classical no-slip conditions are applied, and the surface micro-features specific to owls are not accounted for. In the present computations, the boundary layer thickness just before flow separation at the beginning of the downstroke,
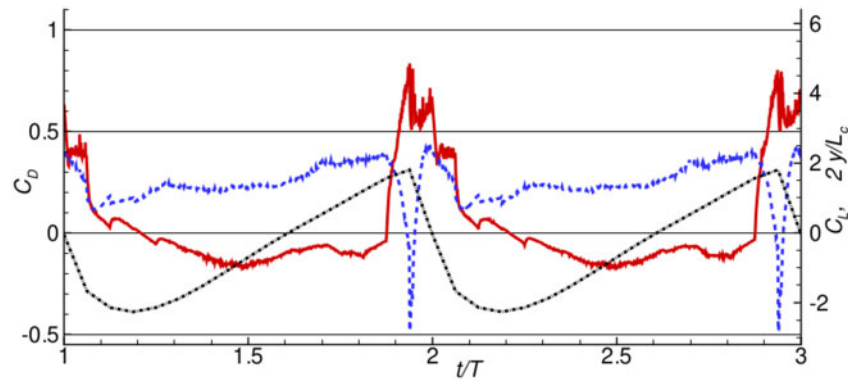
Fig. 10 History of the drag coefficient C_D (left axis), lift coefficient C_L (right axis) and wing tip coordinate (right axis). Medium grid. Lines represent - -; drag coefficient C_D, —; lift coefficient C_L, –·–; y coordinate of wing tip.

for example, measures $\sim$1.5 mm, which is comparable to the thickness of the downy structure ($\sim$2 mm) and leading edge serrations ($\sim$2 − 3 mm). It is, therefore expected that these features will significantly affect the boundary layer development and separation over the wings. As we will demonstrate below, early separation is primarily responsible for the drastic decrease in the lift force.

In particular, Fig. 11 shows contours of the instantaneous spanwise vorticity, ω_z (left) and the pressure coefficient, C_p (right) at a cross-stream plane slicing through the middle of the wing planform. The choice of mid-plane is somewhat arbitrary as the flow momentum changes in three directions, yet, this exploration is beyond the scope of this article. Three phases during the downstroke are selected. The drag and lift forces along with the vertical movement and acceleration of the wing tip are shown as an insert at the top for reference. Note that a vertical dashed line in the subset indicates the wing configuration and its time identification over the wingbeat. The pressure coefficient along the owl cross section is also plotted on subset on the right. The position of the owl and the location of the spanwise plane are shown at the top of each figure. As the wing starts to accelerate downwards the flow separates at the top side and forms a shear layer. The separation point can be qualitatively determined by observing where the vorticity lifts off the surface of the wing and forms a shear layer. This formation is accompanied by strong negative pressure over the wing. The shear layer becomes unstable and rolls up into a series of concentrated regions of vortices. At this phase, the rollers remain close to the upper surface of the wing and generate areas of low pressure toward the leading edge of the wing. On the lower side, the boundary layer remains attached and no vortex shedding is observed. The pressure is high as a result of the downward motion of the wing.

This large pressure difference between the top and bottom surfaces of the wing is responsible for the peak in the lift coefficient. Note that at this position there is also a fair degree of camber at the airfoil section that enhances the above behavior and is responsible for the sharp drop in the drag coefficient.

Near the middle of the downstroke (see Fig. 11b), the wing moves at a maximum vertical speed and the camber is less pronounced than in the previous phase above. The separation point on the top surface is at the leading edge and the shear layer roll-up extends very high. The latter, however, is considerably farther away from the wing and its resulting impact on the surface pressure is small. On the lower surface, the boundary layer remains attached and at the trailing edge vortex roll-up is observed. The pressure on the lower side is still high giving rise to positive lift values. Figure 11c shows the state of the flow toward the end of the downstroke. At this part of the flapping cycle, the wing slows down considerably and vertical wing speed is low. Note that the camber angle is less pronounced than in the previous two instances. The boundary layer on the top surface is still separated at the leading edge, rolling up into vortices that stay close to the wing surface. On the lower side, the boundary layer also separates close to the leading edge. In this instant, the flow resembles that of an airfoil at very small angle of attack airfoil and the flow appears to be more symmetric than in the previous two phases. The value of the pressure on the lower side is gradually reduced as a result of the wing slowing down and the change in camber angle and matches the pressure on the upper side. As a result, the lift force approaches zero at this instant.

Similarly, the corresponding plots at three phases during the upstroke part of the flapping cycle are shown in Fig. 12. At the beginning of the upstroke, the boundary layer on the upper side is attached. On
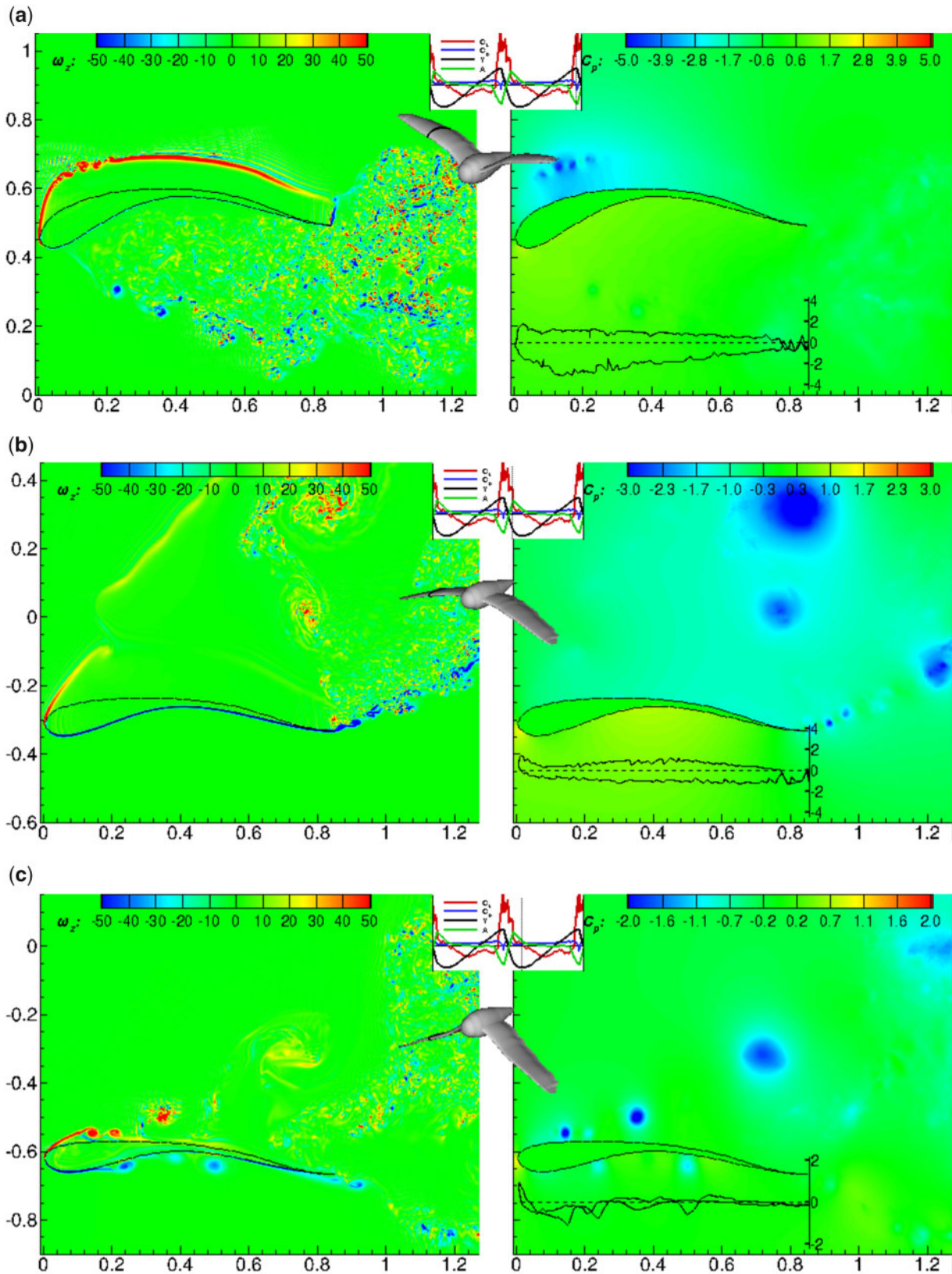
Fig. 11 Contours of the instantaneous spanwise vorticity ω_z (left) and pressure coefficient C_p (right) at a spanwise plane slicing through the middle of the wing at three phases during the downstroke (**a**) $t/T = 0.05$ (**b**) $t/T = 0.15$ $t/T = 0.25$.
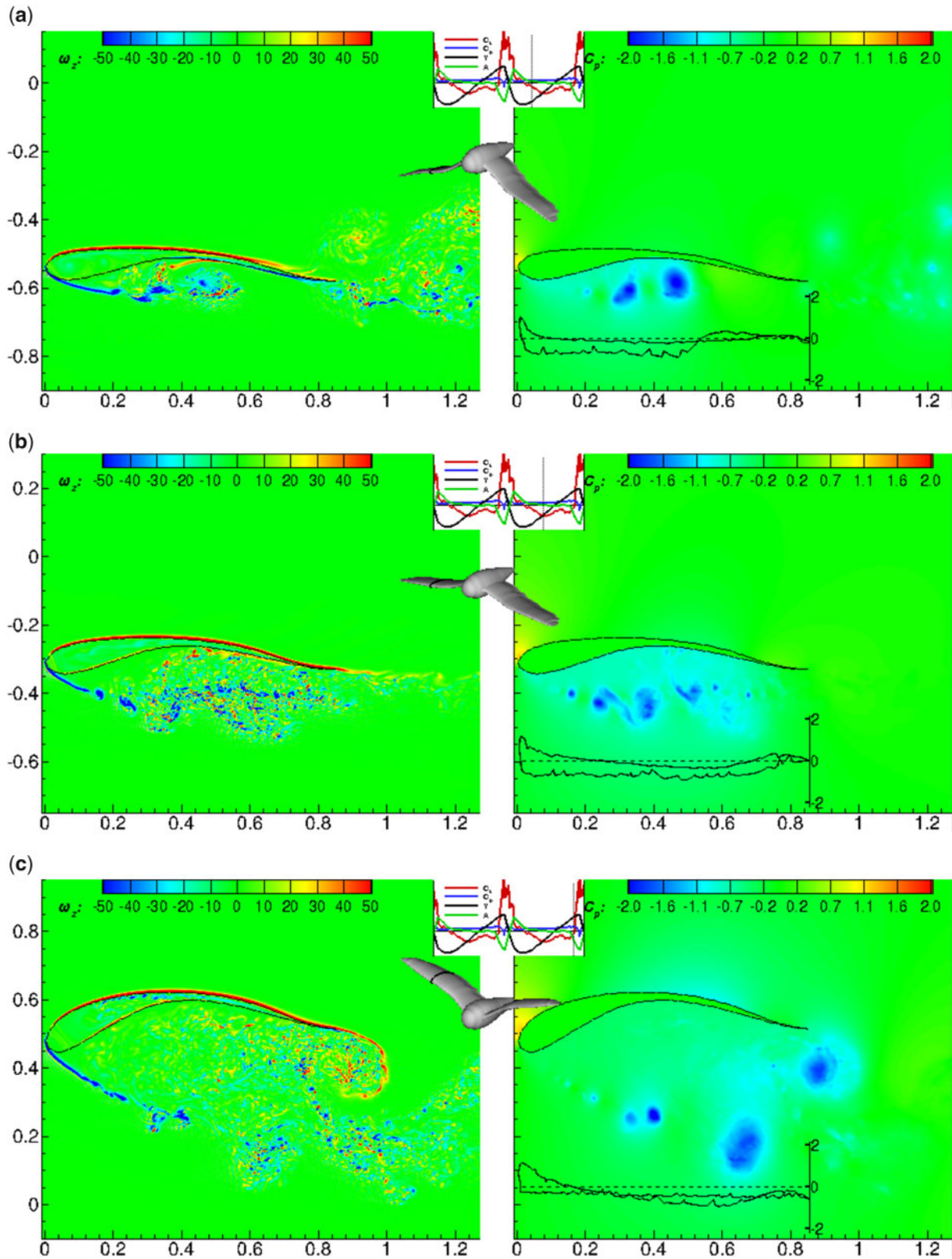
Fig. 12 Contours of the instantaneous spanwise vorticity ω_z and pressure coefficient C_p at a spanwise plane slicing through the middle of the wing at three phases during the downstroke (**a**) $t/T = 0.4$ (**b**) $t/T = 0.6$ $t/T = 0.9$.
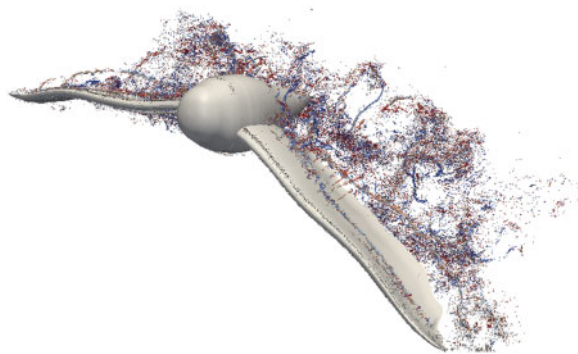
Fig. 13 Instantaneous vortical structures visualized by the Q criterion ($Q = 2.0$) and colored by the streamwise vorticity ω_x near the end of the downstroke.

the lower side of the wing, the boundary layer separates at the leading edge and the shear layer becomes unstable, thus a series of vortices are shed downstream. The vortices remain close to the wing and interact with the lower wing surface near the reattachment point causing the boundary layer to lift off. Due to the reversal of acceleration sign, the pressure on the top is higher than at the bottom and the lift becomes negative. As the wing moves further upward, the flow is qualitatively similar (see Fig. 12b) and the main difference is that change in the camber. The vortices shed from the bottom shear layer stay close to the wing surface creating a region of low pressure. As a result, the pressure on the lower side is consistently lower than on the upper side, causing a further reduction in the lift force. Finally, toward the end of the upstroke shown (see Fig. 12c), the camber increases even more and the wing slows down considerably, which causes the pressure on the upper side to decrease. At the front of the wing the pressure at the top surface is higher than at the bottom while at the trailing edge the behavior is reversed resulting in a zero net effect on the lift. At this phase, a large population of small-scale vortices exists under the wing. They originate from the shear layer roll-up at the leading edge as well as the shear layer forming on the top part of the trailing edge. This phase is followed by transition to downstroke. During the transition phase, one would expect to observe high activity of turbulence, as suggested by Gurka et al. (2017).

A three-dimensional snapshot of the flow at the instant in time near the end of the downstroke is shown in Fig. 13. An iso-surface of the second invariant of the velocity gradient tensor, Q (see Hunt et al. 1988) is used to identify the so-called coherent structures in the turbulent wake. The Q iso-surfaces are colored by the streamwise vorticity, ω_x. The full three-dimensional extend of the vortical structures

resulting from the roll-up of the detached shear layers shown in Figs. 11 and 12 above is visible. These are spanwise rollers forming on both sides of the wing, although in this snapshot only ones on top part are visible. The structures are fairly coherent and cover the entire span of the wing. Initially, just after formation, they are approximately two-dimensional, but as they are convected downstream, they undergo a three dimensional instability and reorient themselves producing structures that resemble Λ-type vortices as indicated on the figure. This is an important mechanism of reorienting the spanwise vorticity produced in the attached boundary layers in the streamwise direction. This is in agreement with the conceptual model by Kroeger et al. (1972), describing the flow evolution developed above an owl wing.

The formation and evolution of all the above flow structures over the wing control the wake flow structure and characteristics. Figure 14, for example, shows contours of the instantaneous vorticity magnitude at four instances during the wing beat cycle. The plane cuts through the middle of the wing and the view is expanded to include the near wake region. The vorticity patterns variations during the upstroke and downstroke parts demonstrate qualitatively the evolution of turbulence in the wake. Vortex shedding is visually observed in the very near wake region followed by growth of the wake and spanning of the vorticity field over the domain. It is also noted that organized shedding of vortices is not apparent downstream of the wake.

Discussion

The aerodynamics of owl flight particularly in relation to their acoustic signature is the result of complex fluid-structure interactions taking place over a wide range of flow scales. As a result, the classical paradigm of independent experiments and computations, no matter how detailed, usually falls short of making advancements in our fundamental understanding the physics. In this study, we propose a strategy utilizing closely coordinated *in vivo* experiments and high fidelity computations that leverages their individual strengths. In particular, the objective of the experiments is to provide the geometry and kinematics of a flying large-sized owl in flapping mode to the simulations. The latter will then provide detailed information on the spatio-temporal flow dynamics including variables that are difficult to measure with sufficient accuracy, such as forces and moments.
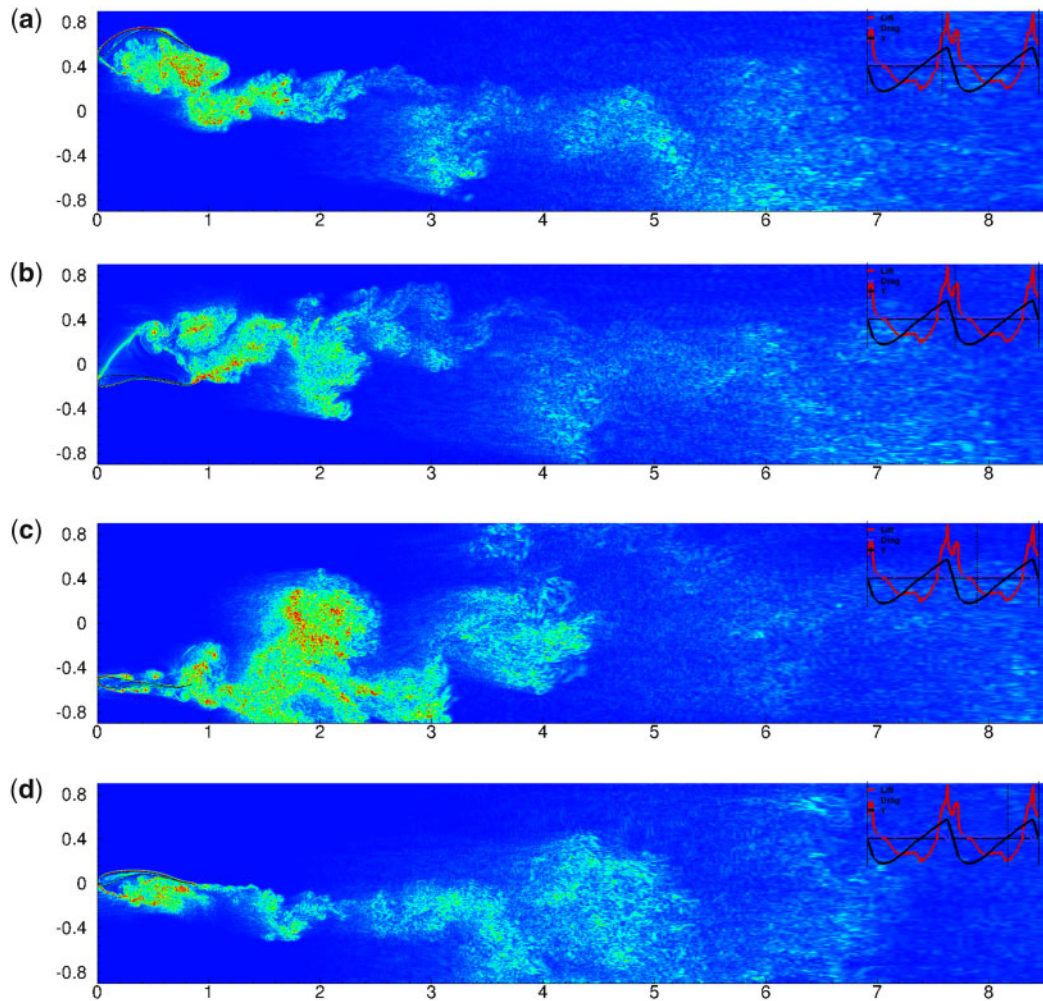
Fig. 14 Contours of (**a**) the instantaneous vorticity magnitude $|\omega|$ at a spanwise plane slicing through the middle of the wing at four phases.

To the best of our knowledge, the computations reported in this study, which utilize billions of degrees of freedom, are the first of this kind, in the pursuit of illuminating the fundamental phenomena behind the silent flight of owls, and in large avian predators' flight in general. Central to the accuracy of such computations is how the geometry and kinematics from *in vivo* experiments are translated into computational models compatible with CFD solvers. Here we propose a novel strategy that uses atlas-driven, image-registration techniques based on the LDDMM framework. The method is very robust in mapping the spatio-temporal evolution of a detailed CAD model of the owl, starting from a reference configuration and the kinematics of a set of markers points on the wing. However, we note that the number and location of these markers has an effect on the fidelity of the reconstructed motion. In this work, we track seven points located at the leading and trailing edge of the wing (see Fig. 7),

which generates some ambiguity in determining the evolution in time of the wing camber. We selected the model parameters to allow dynamic changes that are intuitively physical and have been observed *in vivo*. Reconstructions utilizing a much larger set of points distributed on the wing's surface are needed to quantify more accurately the overall effects.

One of the advantages of such computations when compared to experiments is that the aerodynamic forces can be computed by direct integration of the surface pressure and shear stress. Although this is not a trivial task within the framework of immersed boundary methods, in our earlier work we have demonstrated it can be computed with a high level of confidence (i.e., Rahromostaqim et al. 2016; Wang et al. 2019). The temporal evolution of the lift and drag coefficients reported here is practically independent of the grid resolution, but direct comparisons to the experiments that were the source of the

kinematics are not possible. This is due to the fact that all measurements were extracted from perch-to-perch flight rather than steady flight, limiting the statistical sample to a few flapping cycles and increasing the uncertainties in estimating the aerodynamic forces. Nevertheless, the prediction of the drag force for the present case is in line with experimental observations (Nafi et al. 2020). The changes in drag over the wingbeat cycle include an apparent negative drag during the transition phase, which has been reported by Ben-Gida et al. (2013), associating it to the unsteady drag contribution. The lift coefficient hits a maximum value also during the transition phase from upstroke to downstroke, which has the magnitude expected from this size owls. During the upstroke part of the cycle, however, the lift coefficient drops drastically due to excessive separation of the wing boundary layers. The latter is a strong indication that the adopted smooth surface approximation for the case of owl flight (and bird flight on general) may be a limiting factor in capturing the detailed physics of the boundary layers over the wings which are greatly impacted by the surface micro-features.

The near wake as manifested by the Q-isosurfaces in Fig. 13, and vorticity magnitude in Fig. 14 show a fair degree of coherence and high levels of turbulence and mixing. The strong growth of the wake in the vertical direction, resulting from the shedding of large vortical structures from the leading edge during the transition phase in the cycle, was not observed in experiments involving other owl species (i.e., Lawley et al. 2019). Given that the active or passive deformations of the base wing structure are captured by the proposed computational model we can attribute these differences to the micro-features suggesting that they may also contribute in confining the wake and thus, reducing its momentum.

Acknowledgments

References

Agrawal BR, Sharma A. 2016. Numerical investigations of bio-inspired blade designs to reduce broadband noise in aircraft engines and wind turbines. In Proceedings, 54th AIAA Aerospace Sciences Meeting, January 4–8, 2016, San Diego, CA. p. 0760.

Anderson GW. 1973. An experimental investigation of a high lift device on the owl wing [Master's Thesis]. Air Force Inst. of Tech. Wright-Patterson AFB OH School of Engineering, No. GAM/AE/73-6.

Balaras E. 2004. Modeling complex boundaries using an external force field on fixed cartesian grids in large-eddy simulations. Comput Fluid 33:375–404.

Battley PF, Warnock N, Tibbitts TL, Gill RE Jr, Piersma T, Hassell CJ, Douglas DC, Mulcahy DM, Gartrell BD, Schuckard R, et al. 2012. Contrasting extreme long–distance migration patterns in bar-tailed godwits Limosa lapponica. J Avian Biol 43:21–32.

Beg MF, Miller MI, Trouvé A, Younes L. 2005. Computing large deformation metric mappings via geodesic flows of diffeomorphisms. Int J Comput Vision 61:139–57.

Ben-Gida H, Kirchhefer AJ, Taylor ZJ, Bezner-Kerr W, Guglielmo CG, Kopp GA, Gurka R. 2013. Estimation of unsteady aerodynamics in the wake of a freely flying European starling (Sturnus vulgaris). PLoS One 8:e80086.

Ben-Gida H, Gurka R, Weihs D. 2020. Lift enhancement by a stationary leading-edge vortex over a high aspect ratio wing. AIAA J 58:2806–19.

Clark CJ, Piane KL, Liu L. 2020. Evolution and ecology of silent flight in owls and other flying vertebrates. Integr Organ Biol 2:obaa001.

Dassault-Systemes. Solidworks software description (https://www.solidworks.com).

Deformetrica. Deformetrica software description (http://www.deformetrica.org).

Durrleman S, Prastawa M, Charon N, Korenberg JR, Joshi S, Gerig G, Trouvé A. 2014. Morphometry of anatomical shape complexes with dense deformations and sparse parameters. NeuroImage 101:35–49.

Ford CP, Babinsky H. 2013. Lift and the leading-edge vortex. J Fluid Mech 720:280–313.

Gardiner J, Abdul Razak N, Dimitriadis G, Tickle P, Codd JR, Nudds L. 2013. Simulation of bird wing flapping using the unsteady vortex lattice method. Proceedings of the International Forum on Aeroelasticity and Structural Dynamics, IFASD, June 23–27, 2013, Bristol, UK.

Geyer T, Claus VT, Hall PM, Sarradj E. 2017. Silent owl flight: the effect of the leading edge comb. Int J Aeroacoust 16:115–34.

Geyer TF, Sarradj E, Fritzsche C. 2013. Silent owl flight: comparative acoustic wind tunnel measurements on prepared wings. Acta Acust United Acust 99:139–53.

Gori P, Colliot O, Marrakchi-Kacem L, Worbe Y, Poupon C, Hartmann A, Ayache N, Durrleman S. 2017. A bayesian framework for joint morphometry of surface and curve meshes in multi-object complexes. Med Image Anal 35:458–74.

Graham RR. 1934. The silent flight of owls. Aeronaut J 38:837–43.

Gurka K, Krishnan R, Ben-Gida H, Kirchhefer A, Kopp GA, Guglielmo CG. 2017. Flow pattern similarities in the near wake of three bird species suggest a common role for unsteady aerodynamic effects in lift generation. Interface Focus 7:20160090.

Hedenström A, Norevik G, Warfvinge K, Andersson A, Bäckman J, Åkesson S. 2016. Annual 10-month aerial life phase in the common swift *Apus apus*. Curr Biol 26:3066–70.

Hedrick TL, Usherwood JR, Biewener AA. 2004. Wing inertia and whole-body acceleration: an analysis of instantaneous aerodynamic force production in cockatiels (*Nymphicus hollandicus*) flying across a range of speeds. J Exp Biol 207:1689–702.

Henningsson P, Spedding GR, Hedenström A. 2008. Vortex wake and flight kinematics of a swift in cruising flight in a wind tunnel. J Exp Biol 211:717–30.

Hunt JCR, Wray A, Moin P. 1988. Eddies, streams, and convergence zones in turbulent flows. Stud Turbuleng Numer Simul Data 1:193–208.

Kirchhefer AJ, Kopp GA, Gurka R. 2013. The near wake of a freely flying European starling. Phys Fluids 25:051902.

König C, Weick F. 2008. A Owls of the world. London: A & C Black.

Kondo K, Aono H, Nonomura T, Anyoji M, Oyama A, Liu T, Fujii K, Yamamoto M. 2014. Analysis of owl-like airfoil aerodynamics at low Reynolds number flow. Transact Jpn Soc Aeronaut Space Sci Aerospace Technol Jpn 12:Tk_35–40.

Kroeger RA, Grushka HD, Helvey TC. 1972. Low speed aerodynamics for ultra-quiet flight. Technical Report. Ohio: Air Force Flight Dynamics Laboratory, Wright Patterson Airforce Base. AFFDL-TR-71-75. p. 1–55.

Lawley J, Ben-Gida H, Krishnamoorthy K, Hackett EE, Kopp GA, Morgan G, Guglielmo CG, Gurka R. 2019. Flow features of the near wake of the Australian boobook owl (*Ninox boobook*) during flapping flight suggest an aerodynamic mechanism of sound suppression for stealthy flight. Integr Organ Biol 1:obz001.

Liu T, Kuykendoll K, Rhew R, Jones S. 2006. Avian wing geometry and kinematics. AIAA J 44:954–63.

Mansi T, Voigt I, Leonardi B, Pennec X, Durrleman S, Sermesant M, Delingette H, Taylor AM, Boudjemline Y, Pongiglione G, et al. 2011. A statistical model for quantification and prediction of cardiac remodelling: application to Tetralogy of Fallot. IEEE Transact Med Imag 30:1605–16.

Moin P, Mahesh K. 1998. Direct numerical simulation: a tool in turbulence research. Ann Rev Fluid Mech 30:539–78.

Nafi A, Ben-Gida H, Guglielmo CG, Gurka R. 2020. Aerodynamic forces acting on birds during flight: a comparative study of a shorebird, songbird and a strigiform. Exp Thermal Fluid Sci 113:110018.

OpenFoam. 2007. OpenFoam—the open source CFD toolbox—user's guide. 1.4th ed. Bracknell: OpenCFD Ltd.

Orlanski I. 1976. A simple boundary condition for unbounded hyperbolic flows. J Comput Phys 21:251–69.

Pal A, Sarkar S, Posa A, Balaras E. 2017. Direct numerical simulation of stratified flow past a sphere at a subcritical Reynolds number of 3700 and moderate Froude number. J Fluid Mech Anics 826:5–31.

Pope SB. 2011. Turbulent flows. Cambridge: Cambridge University Press.

Posa A, Balaras E. 2016. A numerical investigation of the wake of an axisymmetric body with appendages. J Fluid Mech 792:470–98. –

Posa A, Balaras E. 2018. Large Eddy Simulation of an isolated vertical axis wind turbine. J Wind Eng Ind Aerodynam 172:139–51.

Posa A, Parker CM, Leftwich MC, Balaras E. 2016. Wake structure of a single vertical axis wind turbine. Int J Heat Fluid Flow 61:75–84.

Posa A, Vanella M, Balaras E. 2017. An adaptive reconstruction for Lagrangian, direct-forcing, immersed-boundary methods. J Comput Phys 351:422–36.

Rahromostaqim M, Posa A, Balaras E. 2016. Numerical investigation of the performance of pitching airfoils at high amplitudes. AIAA J 54:2221–32.

Rosén M, Spedding GR, Hedenström A. 2007. Wake structure and wingbeat kinematics of a house-martin *Delichon urbica*. J Royal Soc Interface 4:659–68.

Ruck S, Oertel H. 2010. Fluid–structure interaction simulation of an avian flight model. J Exp Biol 213:4180–92.

Shyy W, Lian Y, Tang J, Viieru D, Liu H. 2008. Aerodynamics of low Reynolds number flyers. New York (NY): Cambridge University Press.

Skotheim JM, Mahadevan L. 2004. Dynamics of poroelastic filaments. Proc Math Phys Eng Sci 460:1995–2020.

Song J, Luo H, Tobalske B, and Hedrick T. 2016. Three-dimensional numerical simulation of hummingbird forward flight. 46th AIAA Fluid Dynamics Conference, 13–17 June 2016, Washington, DC.

Taylor ZJ, Gurka R, Kopp GA, Liberzon A. 2010. Long-duration time-resolved piv to study unsteady aerodynamics. IEEE Transact Instrument Measure 59:3262–9.

Tobalske BW, Peacock WL, Dial KP. 1999. Kinematics of flap-bounding flight in the zebra finch over a wide range of speeds. J Exp Biol 202:1725–39.

Wagner H, Weger M, Klaas M, Schröder W. 2017. Features of owl wings that promote silent flight. Interface Focus 7:20160078.

Wang S, Vanella M, Balaras E. 2019. A hydrodynamic stress model for simulating turbulence/particle interactions with immersed boundary methods. J Comput Phys 382:240–63.

Winzen A, Roidl B, Schröder W. 2015. Particle-image velocimetry investigation of the fluid-structure interaction mechanisms of a natural owl wing. Bioinspir Biomim 10:056009.

X-Foil. XFLR5 software description. (www.xflr5.tech/xflr5. htm).

Yang J, Balaras E. 2006. An embedded-boundary formulation for large-eddy simulation of turbulent flows interacting with moving boundaries. J Comput Phys 215:12–40.

Yang SL, Spedding GR. 2013. Separation control by external acoustic excitation at low Reynolds numbers. AIAA J 51:1506–15.